RSC Advances

PAPER

View Article Online
View Journal | View Issue

Cite this: *RSC Adv.*, 2017, **7**, 17586

Combinatorial optimization of the atomic compositions for green-emitting $YBO_3:Ce^{3+},Tb^{3+}$ and red-emitting $YBO_3:Ce^{3+},Tb^{3+},Eu^{3+}$ phosphors using a microplate reader†

Kohei Yano, Satoru Takeshita,‡ Yoshiki Iso* and Tetsuhiko Isobe*

Received 2nd February 2017
Accepted 15th March 2017

DOI: 10.1039/c7ra01356f

rsc.li/rsc-advances

Microplate readers are versatile devices that can rapidly measure the photoluminescence intensities of multiple samples, and are widely used in biological chemistry. In this work, using a commercial microplate reader, we attempted to optimize the atomic compositions of green-emitting phosphor $Y_{1-x-y}Ce_xTb_yBO_3$ and red-emitting phosphor $Y_{1-x-y-z}Ce_xTb_yEu_zBO_3$. We filled 48 individual wells of an alumina microplate with aqueous solutions of nitrates of Y^{3+}, Ce^{3+}, Tb^{3+}, and Eu^{3+} with different compositions, and then added an aqueous solution of boric acid to each well. After drying, the microplate was heated at 550 °C for 2 h in air, and then at 1100 °C for 3 h in a reducing atmosphere. $Y_{1-x-y}Ce_xTb_yBO_3$ absorbed near ultraviolet light through 4f → 5d transitions of Ce^{3+} and emitted green fluorescence corresponding to 4f → 4f transitions of Tb^{3+} through Ce^{3+} → Tb^{3+} energy transfer. Moreover, $Y_{1-x-y-z}Ce_xTb_yEu_zBO_3$ emitted red fluorescence corresponding to 4f → 4f transitions of Eu^{3+} through Ce^{3+} → Tb^{3+} → Eu^{3+} energy transfer under near-ultraviolet light. Measurement of the photoluminescence intensity of each well by a microplate reader revealed that the optimized green and red phosphors were $Y_{0.835}Ce_{0.025}Tb_{0.14}BO_3$ and $Y_{0.535}Ce_{0.005}Tb_{0.45}Eu_{0.01}BO_3$, respectively.

1 Introduction

Luminescent inorganic materials are widely used in various optoelectronic devices and bioassays, such as white light-emitting diodes (LEDs),[1–5] displays,[6] and biological labels,[7–10] because of their high durability and thermal and chemical stabilities. Phosphors that emit visible colors under near-ultraviolet (near-UV) or blue excitation light are currently used as spectral conversion materials in white LEDs. White LEDs composed of a blue-emitting LED and $Y_3Al_5O_{12}$(YAG):Ce^{3+} phosphor that converts blue light to yellow are widely available.[11] However, this conventional combination exhibits a low color rendering index (CRI) because of the lack of a red component. Accordingly, red-emitting phosphors excited by blue LEDs have been used to improve the CRI of devices.[3] White LEDs consisting of a near-UV LED and blue-, green-, and red-emitting phosphors have also been developed.[3] Conventional red phosphors such as Y_2O_3:Eu^{3+} and Y_2O_2S:Eu^{3+} show poor photoluminescence (PL) efficiency under near-UV excitation.[12–15] The absorbance of these phosphors are small in the near-UV region because 4f → 4f transitions of Eu^{3+} are forbidden and their line widths are narrow.[16] To realize efficient red emission of Eu^{3+}, sensitizers with broad and strong absorption in the near-UV region are needed.

YBO_3 is used as a host crystal because of its high transparency and excellent optical damage threshold in the UV and visible regions.[17–20] YBO_3 has been synthesized *via* a solid-state reaction at high temperature.[21] In addition, YBO_3 has also been synthesized at low temperature by combustion,[22,23,28] spray pyrolysis,[24–27] the sol–gel method,[28–33] and coprecipitation.[34,35] Nohara *et al.* and Sato *et al.*[36–38] reported that $YBO_3:Ce^{3+},Tb^{3+}$ emits green light through Ce^{3+} → Tb^{3+} energy transfer under near-UV excitation. Setlur and colleagues found that $YBO_3:Ce^{3+},Tb^{3+},Eu^{3+}$ emits red light *via* Ce^{3+} → Tb^{3+} → Eu^{3+} energy transfer under near-UV excitation.[39] Sohal and co-workers reported that the PL intensities of Ce^{3+} and Tb^{3+} decreased and that of Eu^{3+} increased with increasing Tb^{3+} concentration in $YBO_3:Ce^{3+},Tb^{3+},Eu^{3+}$ at fixed concentrations of Ce^{3+} and Eu^{3+}.[40] The intensity ratio of red emission corresponding to the electric

Department of Applied Chemistry, Faculty of Science and Technology, Keio University, 3-14-1 Hiyoshi, Kohoku-ku, Yokohama 223-8522, Japan. E-mail: iso@applc.keio.ac.jp; isobe@applc.keio.ac.jp; Fax: +81 45 566 1551; Tel: +81 45 566 1558; +81 45 566 1554

† Electronic supplementary information (ESI) available: XRD profiles, crystallite sizes, and actual metallic compositions of the samples taken from the libraries of $Y_{1-x-y}Ce_xTb_yBO_3$ ($0 \le x \le 0.1$, $0 \le y \le 0.4$) (Fig. S1 and Table S1), $Y_{1-x-y-z}Ce_xTb_yEu_zBO_3$ ($0 \le x \le 0.05$, $0 \le y \le 0.90$, $z = 0.05$) (Fig. S2 and Table S2), and $Y_{1-x-y-z}Ce_xTb_yEu_zBO_3$ ($x = 0.005$, $0 \le y \le 0.795$, $0 \le z \le 0.20$) (Fig. S3 and Table S3); PL spectra of $Y_{0.845}Ce_{0.005}Tb_{0.15}BO_3$ and $Y_{0.82}Ce_{0.005}Tb_{0.15}Eu_{0.025}BO_3$ synthesized in the wells of a microplate (Fig. S4); PL and PLE spectra, and CIE coordinate with a color diagram of $Y_{0.535}Ce_{0.005}Tb_{0.45}Eu_{0.01}BO_3$ (Fig. S5). See DOI: 10.1039/c7ra01356f

‡ Research Institute for Chemical Process Technology, National Institute of Advanced Industrial Science and Technology (AIST), Tsukuba Central 5, 1-1-1 Higashi, Tsukuba, Ibaraki 305-8565, Japan E-mail: s.takeshita@aist.go.jp.

dipole transition ($^5D_0 \rightarrow {}^7F_2$) relative to orange emission corresponding to the magnetic dipole transition ($^5D_0 \rightarrow {}^7F_1$) was improved because of the highly distorted symmetry around the Eu^{3+} local site. YBO_3:Ce^{3+},Tb^{3+} and YBO_3:Ce^{3+},Tb^{3+},Eu^{3+} have various relaxation routes whose probabilities depend on the concentrations of individual dopants. For YBO_3:Ce^{3+},Eu^{3+}, the Eu^{3+} emission is quenched by metal-to-metal charge transfer (MMCT) from Ce^{3+} to Eu^{3+} to form Ce^{4+} and Eu^{2+} under near-UV excitation.[39] When YBO_3:Ce^{3+},Eu^{3+} is codoped with a high concentration of Tb^{3+}, Ce^{3+} absorbs near-UV light through the 4f $\rightarrow$ 5d transition, and then sequential energy transfer occurs from Ce^{3+} to Tb^{3+} to Eu^{3+}, followed by red emission from Eu^{3+}.

The combinatorial method is used to fabricate multiple products called a "library" by reacting various combinations of feedstocks. The library is analyzed to identify an optimal product. This method can drastically shorten the time for experimental planning, execution, and analysis. In recent years, combinatorial chemistry has been widely used for drug analysis and synthesis of functional inorganic materials including fluorescent compounds.[41–47] Chen *et al.*[46] developed a unique drop-on-demand inkjet delivery system, which they used to optimize the composition of red-emitting phosphor Y_2O_3:Bi^{3+},Eu^{3+}. Su and colleagues determined the optimum composition of yellow-emitting phosphor $(Lu_{1-x}Gd_x)_3Al_5O_{12}$:$Ce_{3y}$ through a combinatorial procedure.[47] However, these methods used custom-made equipment to analyze each sample in the libraries.

Microplate readers are common commercial devices often used to simultaneously measure the fluorescence intensities of a number of samples, *e.g.*, fluorescently-labeled biomolecules, in a library.[48–50] As a result, microplate readers can drastically shorten analysis time. In this work, we attempt to optimize the atomic compositions of green-emitting phosphor YBO_3:Ce^{3+},Tb^{3+} and red-emitting phosphor YBO_3:Ce^{3+},Tb^{3+},Eu^{3+} excited by near-UV irradiation through combinatorial synthesis and simultaneous analysis using a microplate reader.

2 Experimental section

2.1 Preparation of YBO_3:Ce^{3+},Tb^{3+} and YBO_3:Ce^{3+},Tb^{3+},Eu^{3+} libraries

Yttrium(III) nitrate hexahydrate (Kanto, 99.99%), cerium(III) nitrate hexahydrate (Kanto, 98.5%), terbium(III) nitrate hexahydrate (Kanto, 99.95%), and europium(III) nitrate hexahydrate (Kanto, 99.99%) were dissolved in ultrapure water to prepare 0.5 M aqueous solutions of $RE(NO_3)_3$ (RE = Y, Ce, Tb, Eu). Boric acid (Aldrich, 99.99%) was dissolved in ultrapure water to prepare a 0.6 M aqueous solution. Each of the 48 wells of an alumina microplate was filled with an aqueous nitrate solution (1 mL), which is a mixture of the prepared $RE(NO_3)_3$ solutions with a desired ratio and boric acid (4 mL), and then the microplate was dried at 80 °C. This process was repeated five times by human hands. After drying, the 48 mixtures in the microplate were ground by human hands and pre-heated in a muffle furnace at 550 °C for 2 h in air, following cooling to room temperature. Each sample was reground and then heated at 1100 °C for 3 h in a reducing atmosphere using carbon board to obtain YBO_3:Ce^{3+},Tb^{3+} and YBO_3:Ce^{3+},Tb^{3+},Eu^{3+} phosphors.

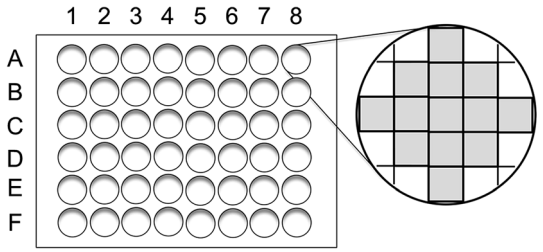

Fig. 1 Division of each well in a microplate into 13 blocks for PL intensity evaluation.

2.2 Characterization

Powder X-ray diffraction (XRD) profiles were measured using an X-ray diffractometer (Rigaku, Rint 2200) with a Cu Kα radiation source. The elemental composition of YBO_3:Ce^{3+},Tb^{3+} and YBO_3:Ce^{3+},Tb^{3+},Eu^{3+} powder samples was determined by the fundamental parameter method using an X-ray fluorescence analyzer (Rigaku, ZSX mini II). Both PL and photoluminescence excitation (PLE) spectra were measured using a fluorescence spectrometer (JASCO, FP-6500) equipped with a 150-W Xe lamp. The PL intensity of each well of the microplate was measured using a multi-detection microplate reader (DS Pharma Biomedical, Powerscan HT) with an excitation band-pass filter (BT-7082220; 360 $\pm$ 40 nm). Emission band-pass filters [BT-7082210 (545 $\pm$ 40 nm) and BT-7082226 (645 $\pm$ 40 nm)] were used to detect green and red emission, respectively. Each well of a microplate was divided to 13 blocks, as shown in Fig. 1, and the PL intensity of each well was defined as an average of three strongest PL intensity among the 13 blocks. The PL measurement of 48 wells was completed in ~8 min. To determine the precision of the procedure, $Y_{0.82}Ce_{0.03}Tb_{0.15}BO_3$ was synthesized in 48 wells of a microplate and the PL intensity of each well was evaluated from a representative value, which was the average of the three highest PL intensities among 13 blocks. The relative deviation of representative values of PL intensities was within 8.0%.

3 Results and discussion

3.1 Structural properties of the $Y_{1-x-y}Ce_xTb_yBO_3$ library

XRD profiles of samples from the $Y_{1-x-y}Ce_xTb_yBO_3$ library ($0 \leq x \leq 0.1$, $0 \leq y \leq 0.4$) with a wide range of Ce^{3+} and Tb^{3+} concentrations synthesized in the wells of a microplate were measured (see Fig. S1†). All the XRD peaks except for that at 27.5° belonged to YBO_3 with hexagonal structure. The peak at 27.5° possibly originated from the byproduct Y_3BO_6, which accidentally formed through the evaporation of boron. Actual metallic compositions of typical samples (shown in Table S1†) were evaluated to be close to loading ones except for that of the sample taken from well A-7.

3.2 Photoluminescence spectra of the $Y_{1-x-y}Ce_xTb_yBO_3$ library

Fig. 2 shows PL and PLE spectra of $Y_{0.98}Ce_{0.02}BO_3$ and $Y_{0.83}Ce_{0.02}Tb_{0.15}BO_3$ synthesized in the wells of a microplate. The

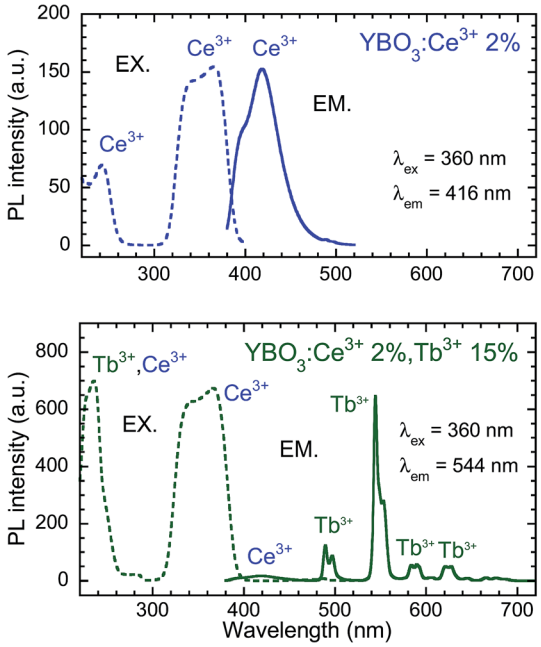

Fig. 2 PL and PLE spectra of $Y_{0.98}Ce_{0.02}BO_3$ and $Y_{0.83}Ce_{0.02}Tb_{0.15}BO_3$ synthesized in the wells of a microplate.

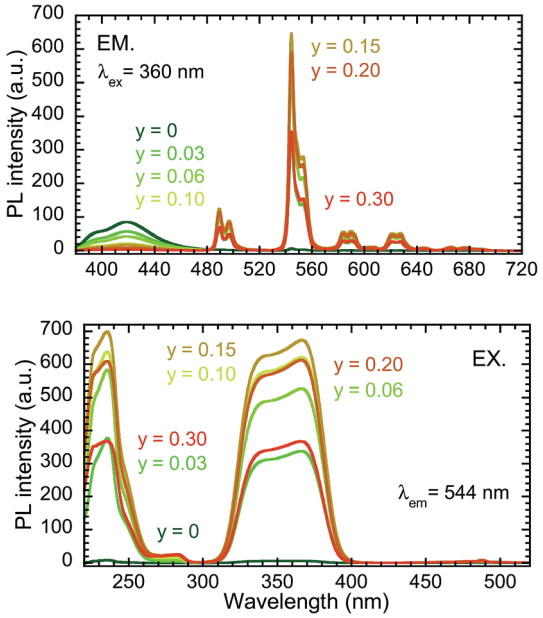

Fig. 3 PL and PLE spectra of samples from the $Y_{0.98-y}Ce_{0.02}Tb_yBO_3$ library ($0 \le y \le 0.3$).

PL intensity at 416 nm corresponding to the 5d → 4f transition of Ce^{3+} for $Y_{0.83}Ce_{0.02}Tb_{0.15}BO_3$, which exhibited Tb^{3+} emission in the wavelength region of 480–640 nm, was lower than that for $Y_{0.98}Ce_{0.02}BO_3$. In the PLE spectrum of $Y_{0.83}Ce_{0.02}Tb_{0.15}BO_3$ monitored at the Tb^{3+} $^5D_4 \rightarrow {}^7F_5$ emission wavelength λ_{em} of 544 nm, the excitation peak corresponding to the 4f → 5d transition of Ce^{3+} was observed at 360 nm. This result indicates that energy transfer occurred from Ce^{3+} to Tb^{3+}.

Fig. 3 depicts the PL (excitation wavelength $\lambda_{ex} = 360$ nm) and PLE ($\lambda_{em} = 544$ nm) spectra of the samples from the $Y_{0.98-y}Ce_{0.02}Tb_yBO_3$ library, in which the Ce^{3+} concentration was fixed at 2 at% and the Tb^{3+} concentration was varied from 0 to 30 at%. The maximum PL intensity at 544 nm corresponding to the $^5D_4 \rightarrow {}^7F_5$ transition of Tb^{3+} was observed when the Tb^{3+} concentration was 15 at%. The PL intensity of the Ce^{3+} 5d → 4f emission simply decreased with increasing Tb^{3+} concentration. The efficiency of $Ce^{3+} \rightarrow Tb^{3+}$ energy transfer and PL intensity of the Tb^{3+} $^5D_4 \rightarrow {}^7F_5$ emission at 544 nm are plotted as a function of Tb^{3+} concentration in Fig. 4. Energy transfer efficiency, η, is given by:

$$\eta = 1 - \frac{I}{I_0} \quad (1)$$

where I_0 and I are the PL intensities of Ce^{3+} at 416 nm in the absence and presence of Tb^{3+}, respectively.[51] The PL intensity of Tb^{3+} increased with η and reached its maximum value when the Tb^{3+} concentration was 15 at%. Over 15 at% Tb^{3+}, η approached unity, and the PL intensity of Tb^{3+} decreased. This decrease is attributed to concentration quenching of Tb^{3+} due to enhancement of probability of a non-radiative relaxation through the energy migration of $Tb^{3+} \rightarrow Tb^{3+}$.

3.3 Optimization of the atomic composition of the $Y_{1-x-y}Ce_xTb_yBO_3$ phosphor

To roughly determine the optimum atomic composition range of the $Y_{1-x-y}Ce_xTb_yBO_3$ phosphor, a $Y_{1-x-y}Ce_xTb_yBO_3$ library with various Ce^{3+} and Tb^{3+} concentrations over wide ranges of $0 \le x \le 0.1$ and $0 \le y \le 0.4$ was prepared. Fig. 5(a) shows a fluorescence image of the library under near-UV excitation and measured PL intensities of each well measured by the microplate reader. Strong emission was observed when the Ce^{3+} concentration was 2–3 at% and Tb^{3+} concentration was 15 at%.

Next, a $Y_{1-x-y}Ce_xTb_yBO_3$ library with narrow ranges of $0.020 \le x \le 0.045$ and $0.02 \le y \le 0.16$ was prepared to find the optimum atomic composition for this phosphor. As illustrated

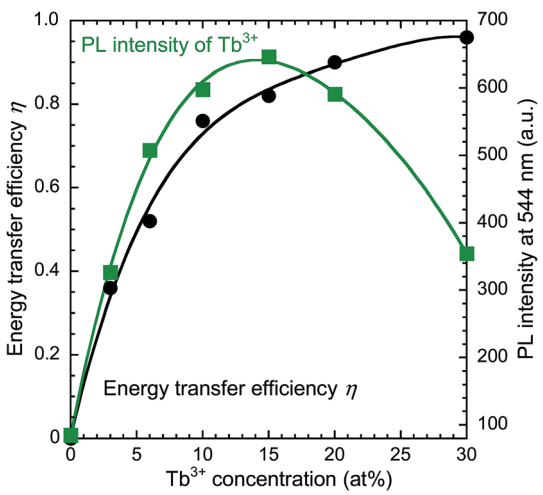

Fig. 4 Dependence of the energy transfer efficiency and PL intensity of $Y_{0.98-y}Ce_{0.02}Tb_yBO_3$ ($0 \le y \le 0.3$) samples on Tb^{3+} concentration.

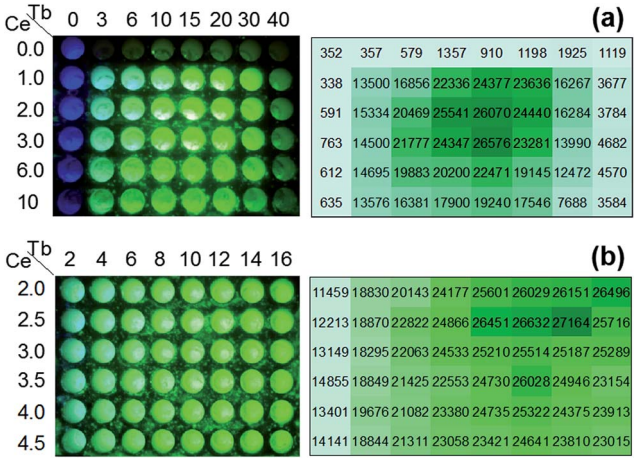

Fig. 5 Fluorescent images of $Y_{1-x-y}Ce_xTb_yBO_3$ libraries under near-UV excitation and values of green emission intensity (λ_{ex} = 360 nm) in each well measured by a microplate reader. $Y_{1-x-y}Ce_xTb_yBO_3$ libraries with (a) ($0 \le x \le 0.10$, $0 \le y \le 0.40$) and (b) ($0.020 \le x \le 0.045$, $0.02 \le y \le 0.16$).

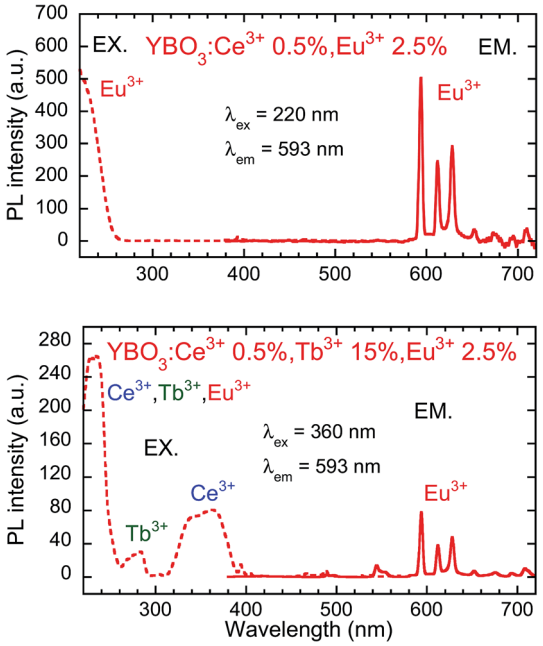

Fig. 6 PL and PLE spectra of $Y_{0.97}Ce_{0.005}Eu_{0.025}BO_3$ and $Y_{0.82}Ce_{0.005}Tb_{0.15}Eu_{0.025}BO_3$.

in Fig. 5(b), $Y_{0.835}Ce_{0.025}Tb_{0.14}BO_3$ was determined as the optimum composition with the strongest green PL intensity.

3.4 Structural properties of the $Y_{1-x-y-z}Ce_xTb_yEu_zBO_3$ library

XRD profiles of samples from the $Y_{1-x-y-z}Ce_xTb_yEu_zBO_3$ library ($0 \le x \le 0.05$, $0 \le y \le 0.90$, $z = 0.05$; synthesized with wide ranges of Ce^{3+} and Tb^{3+} concentrations and a fixed Eu^{3+} concentration of 5 at%) and $Y_{1-x-y-z}Ce_xTb_yEu_zBO_3$ library ($x = 0.005$, $0 \le y \le 0.795$, $0 \le z \le 0.20$; synthesized with wide ranges of Tb^{3+} and Eu^{3+} concentrations and a fixed Ce^{3+} concentration of 0.5 at%) were measured (see Fig. S2 and S3,† respectively). All the XRD peaks except for a weak peak attributed to Y_3BO_6 at 27.5° belonged to YBO_3 with hexagonal structure. Actual metallic compositions were close to loading ones (see Tables S2 and S3†).

3.5 Photoluminescence spectra of the $Y_{1-x-y-z}Ce_xTb_yEu_zBO_3$ library

Fig. 6 presents PL and PLE spectra of $Y_{0.97}Ce_{0.005}Eu_{0.025}BO_3$ and $Y_{0.82}Ce_{0.005}Tb_{0.15}Eu_{0.025}BO_3$ synthesized in the wells of a microplate. In the PLE spectrum monitored at the Eu^{3+} $^5D_0 \rightarrow {}^7F_1$ emission (λ_{em} = 593 nm), the excitation peak corresponding to the 4f → 5d transition of Ce^{3+} was not observed for $Y_{0.97}Ce_{0.005}Eu_{0.025}BO_3$. In contrast, for $Y_{0.82}Ce_{0.005}Tb_{0.15}Eu_{0.025}BO_3$, the excitation peaks ascribed to the Tb^{3+} $4f^8 \rightarrow 4f^75d^1$ and Ce^{3+} 4f → 5d transitions were observed at 280 and 360 nm, respectively. This result indicates that Tb^{3+} relays the energy of excited Ce^{3+} to Eu^{3+}. Judging from the PL spectra of $Y_{0.845}Ce_{0.005}Tb_{0.15}BO_3$ and $Y_{0.82}Ce_{0.005}Tb_{0.15}Eu_{0.025}BO_3$ synthesized in the wells of a microplate (Fig. S4†), PL intensities of Tb^{3+} and Ce^{3+} under excitation of Ce^{3+} decreased after co-doping with Eu^{3+}, indicating that $Ce^{3+} \rightarrow Eu^{3+}$ and $Ce^{3+} \rightarrow Tb^{3+} \rightarrow Eu^{3+}$ energy transfer processes occurred. However, $Ce^{3+} \rightarrow Eu^{3+}$ direct energy transfer did not contribute to the Eu^{3+} emission, because MMCT caused Ce^{3+} and Eu^{3+} to convert to Ce^{4+} and Eu^{2+}, respectively, quenching the Eu^{3+} emission.

Fig. 7 shows the PL (λ_{ex} = 360 nm) and PLE (λ_{em} = 593 nm) spectra of samples from the $Y_{0.845-z}Ce_{0.005}Tb_{0.15}Eu_zBO_3$ library, in which Ce^{3+} and Tb^{3+} concentrations were fixed at 0.5 and 15 at%, respectively, and Eu^{3+} concentration was varied from 0 to 20 at%. The maximum PL intensity of Eu^{3+} at 593 nm was reached at an Eu^{3+} concentration of 2.5 at%. The PL intensity of Tb^{3+} decreased with increasing Eu^{3+} concentration. $Tb^{3+} \rightarrow Eu^{3+}$ energy transfer efficiency and the PL intensity of Eu^{3+} at 593 nm are plotted as a function of Eu^{3+} concentration in Fig. 8. The η of $Tb^{3+} \rightarrow Eu^{3+}$ energy transfer was estimated using eqn (1); in this case, I_0 and I were the PL intensities of Tb^{3+} at 544 nm in the absence and presence of Eu^{3+}, respectively. With increasing Eu^{3+} concentration, η increased until it approached unity over an Eu^{3+} concentration of 2.5 at%, while the PL intensity of Eu^{3+} decreased over this concentration. This result would indicate that concentration quenching of Eu^{3+},[52,53] caused by enhancement of probability of a non-radiative relaxation through the energy migration of $Eu^{3+} \rightarrow Eu^{3+}$, occurred when the Eu^{3+} concentration exceeded 2.5 at%. It should be noted that the MMCT effect between Ce^{3+} and Eu^{3+} was ignored for the calculation of η. The decrease in PL intensity might be affected by enhancement of the MMCT as well as the concentration quenching.

3.6 Optimization of the atomic composition of the $Y_{1-x-y-z}Ce_xTb_yEu_zBO_3$ phosphor

To roughly determine the optimum concentration range of the $Y_{1-x-y-z}Ce_xTb_yEu_zBO_3$ phosphor, a $Y_{1-x-y-z}Ce_xTb_yEu_zBO_3$ library with various Ce^{3+} and Tb^{3+} concentrations over wide

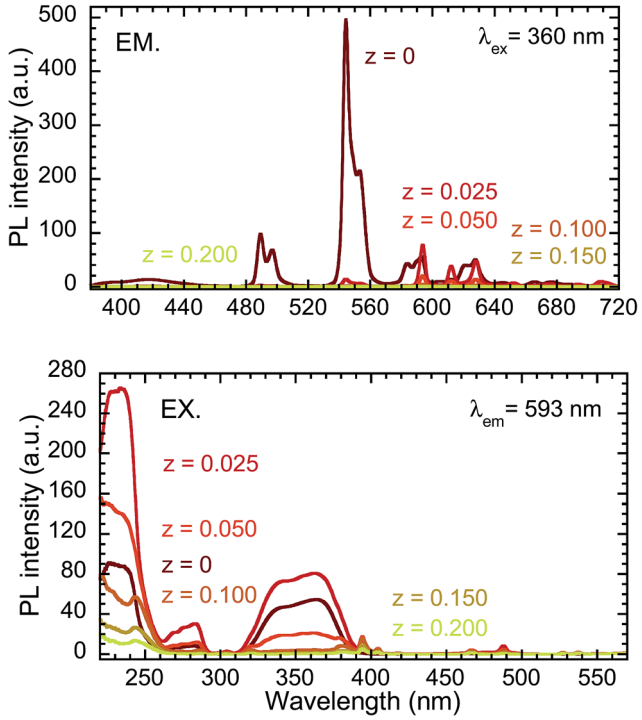

Fig. 7 PL and PLE spectra of samples from the $Y_{0.845-z}Ce_{0.005}Tb_{0.15}Eu_zBO_3$ library ($0 \le z \le 0.2$).

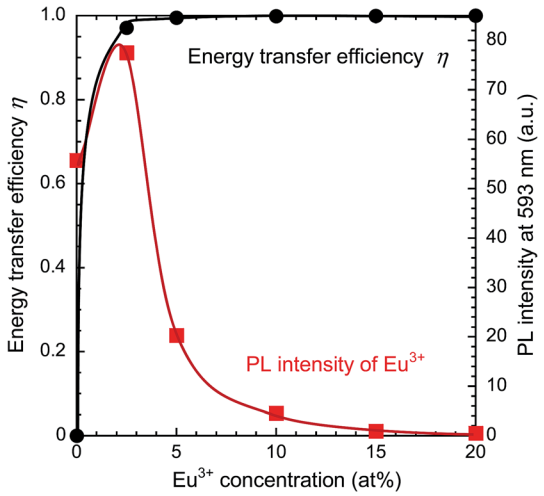

Fig. 8 Dependence of the energy transfer efficiency and PL intensity of $Y_{0.845-z}Ce_{0.005}Tb_{0.15}Eu_zBO_3$ ($0 \le z \le 0.2$) on Eu^{3+} concentration.

ranges of $0 \le x \le 0.05$ and $0 \le y \le 0.90$ and a fixed Eu^{3+} concentration of 5 at% was prepared. Fig. 9(a) shows a fluorescence image of the library under near-UV excitation and the average value of the three strongest red emission intensities in each well measured by a microplate reader. The strong emission was observed for Ce^{3+} and Tb^{3+} concentrations of 0–2 and 40–90 at%, respectively. To determine the optimum concentration of Ce^{3+}, a $Y_{1-x-y-z}Ce_xTb_yEu_zBO_3$ library with narrow ranges of $0 \le x \le 0.025$ and $0.34 \le y \le 0.90$ and at a fixed Eu^{3+} concentration of 5 at% was prepared. As illustrated in Fig. 9(b), the strong

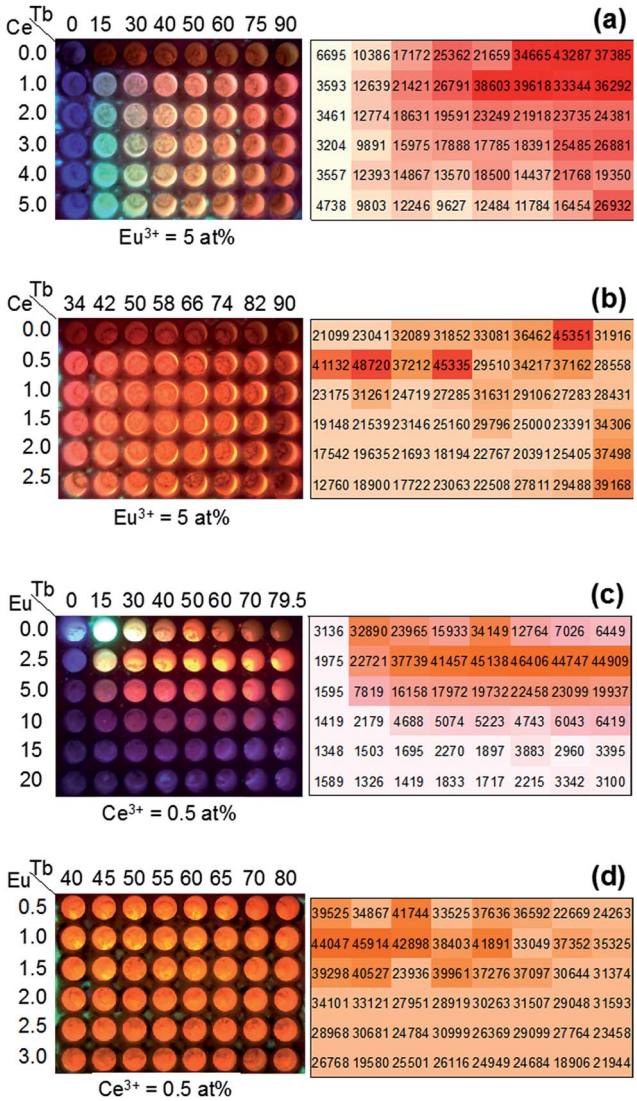

Fig. 9 Fluorescent images of $Y_{1-x-y-z}Ce_xTb_yEu_zBO_3$ libraries under near-UV excitation and values of red emission intensity ($\lambda_{ex} = 360$ nm) in each well measured by a microplate reader. $Y_{1-x-y-z}Ce_xTb_yEu_zBO_3$ libraries with (a) ($0 \le x \le 0.05$, $0 \le y \le 0.90$, $z = 0.05$), (b) ($0 \le x \le 0.025$, $0.34 \le y \le 0.90$, $z = 0.05$), (c) ($x = 0.005$, $0 \le y \le 0.795$, $0 \le z \le 0.20$), and (d) ($x = 0.005$, $0.40 \le y \le 0.80$, $0.005 \le z \le 0.030$).

emission was found when the concentrations of Ce^{3+} and Tb^{3+} were 0.5 at% and 40–60 at%, respectively. Therefore, the optimum concentration of Ce^{3+} was 0.5 at%.

A $Y_{1-x-y-z}Ce_xTb_yEu_zBO_3$ library with wide concentration ranges of $0 \le y \le 0.795$ and $0 \le z \le 0.20$ and at a fixed Ce^{3+} concentration of 0.5 at% was prepared. Fig. 9(c) reveals that strong emission was obtained for concentrations of Tb^{3+} of 40–80 at% and Eu^{3+} of 2.5 at%. Then, a $Y_{1-x-y-z}Ce_xTb_yEu_zBO_3$ library with narrow ranges of $0.40 \le y \le 0.80$ and $0.005 \le z \le 0.030$ and a fixed Ce^{3+} concentration of 0.5 at% was prepared to determine the optimum composition of this phosphor. Fig. 9(d) indicates that $Y_{0.535}Ce_{0.005}Tb_{0.45}Eu_{0.01}BO_3$ is the optimum composition with the strongest red PL intensity. Red to orange ratios were calculated from the PL intensities attributed to $^5D_0 \rightarrow {}^7F_1$ transition (O) at 593 nm and $^5D_0 \rightarrow {}^7F_2$ transition of Eu^{3+}

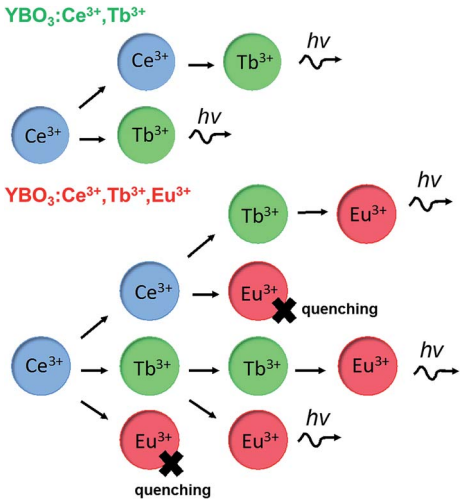

Fig. 10 Schematic illustration of the energy transfer routes in $YBO_3:Ce^{3+},Tb^{3+}$ and $YBO_3:Ce^{3+},Tb^{3+},Eu^{3+}$.

(see PL and PLE spectra shown in Fig. S5†). There were two large red peaks assigned to the $^5D_0 \rightarrow {}^7F_2$ transition at 611 nm (R_1) and 627 nm (R_2) due to Stark splitting. Calculated ratios were $R_1/O = 0.484$ and $R_2/O = 0.621$. CIE coordinate obtained from the PL spectrum was (0.636, 0.359) (also shown in Fig. S5†).

3.7 Factors determining the optimum composition of the $Y_{1-x-y-z}Ce_xTb_yEu_zBO_3$ phosphor

The optimum concentration of Ce^{3+} and Tb^{3+} in $Y_{1-x-y}Ce_xTb_yBO_3$ were 2.5 and 14 at%, respectively. In contrast, the optimum concentrations of Ce^{3+}, Tb^{3+}, and Eu^{3+} in $Y_{1-x-y-z}Ce_xTb_yEu_zBO_3$ were 0.5, 45, and 1.0 at%, respectively. We note that the optimum concentrations of Ce^{3+} and Tb^{3+} for $Y_{1-x-y-z}Ce_xTb_yEu_zBO_3$ were lower and higher, respectively, compared with those in $Y_{1-x-y}Ce_xTb_yBO_3$. This means the addition of Tb^{3+} suppresses the quenching of Eu^{3+} emission by inhibiting MMCT from Ce^{3+} to Eu^{3+} which results from enhancing probability of the $Ce^{3+} \rightarrow Tb^{3+}$ energy transfer. Fig. 10 summarizes energy transfer routes in the phosphors. Because of the lower concentration of Ce^{3+} and higher concentration of Tb^{3+} in $Y_{1-x-y-z}Ce_xTb_yEu_zBO_3$ compared with those in $Y_{1-x-y}Ce_xTb_yBO_3$, the possibility of $Ce^{3+} \rightarrow Tb^{3+}$ energy transfer could be higher than $Ce^{3+} \rightarrow Eu^{3+}$ energy transfer in $Y_{1-x-y-z}Ce_xTb_yEu_zBO_3$.

4 Conclusions

Metal nitrate aqueous solutions with different compositions and boric acid aqueous solution were reacted in alumina microplate wells to obtain libraries of the green-emitting phosphor $Y_{1-x-y}Ce_xTb_yBO_3$ and red-emitting phosphor $Y_{1-x-y-z}Ce_xTb_yEu_zBO_3$. The compositions of both phosphors were optimized by evaluating the PL intensity of each microplate well measured by a versatile microplate reader. For the green-emitting phosphor, the concentrations of Ce^{3+} and Tb^{3+} were changed over wide ranges, and then over narrow ranges. The determined optimum composition of $Y_{1-x-y}Ce_xTb_yBO_3$ was $Y_{0.835}Ce_{0.025}Tb_{0.14}BO_3$. For the red-emitting phosphor, the concentration of Eu^{3+} was fixed at 5 at% and the concentrations of Ce^{3+} and Tb^{3+} were optimized similarly. The PL intensity of this phosphor was more sensitive to Ce^{3+} concentration than Tb^{3+}, and the determined optimum concentration of Ce^{3+} was 0.5 at%. Then, the concentrations of Tb^{3+} and Eu^{3+} were optimized at a constant Ce^{3+} concentration of 0.5 at%. The determined optimum composition of $Y_{1-x-y-z}Ce_xTb_yEu_zBO_3$ was $Y_{0.535}Ce_{0.005}Tb_{0.45}Eu_{0.01}BO_3$. The optimum concentration of Ce^{3+} was lower and that of Tb^{3+} was higher for the red-emitting phosphor compared with those of the green-emitting phosphor. This is attributed to suppression of $Ce^{3+} \rightarrow Eu^{3+}$ MMCT, which causes quenching of Eu^{3+} emission, using a lower Ce^{3+}concentration. The technique developed in this work will be useful to determine the optimum compositions of other phosphors.

References

1 D. A. Steigerwald, J. C. Bhat, D. Collins, R. M. Fletcher, M. O. Holcomb, M. J. Ludowise, P. S. Martin and S. L. Rudaz, *IEEE J. Sel. Top. Quantum Electron.*, 2002, **8**, 310–320.
2 H. A. Höppe, *Angew. Chem., Int. Ed.*, 2009, **48**, 3572–3582.
3 S. Ye, F. Xiao, Y. X. Pan, Y. Y. Ma and Q. Y. Zhang, *Mater. Sci. Eng., R*, 2010, **71**, 1–34.
4 A. Revaux, G. Dantelle, N. George, R. Seshadri, T. Gacoin and J. P. Boilot, *Nanoscale*, 2011, **3**, 2015–2022.
5 W.-Y. Huang, F. Yoshimura, K. Ueda, Y. Shimomura, H.-S. Sheu, T.-S. Chan, H. F. Greer, W. Zhou, S.-F. Hu, R.-S. Liu and J. P. Attfield, *Angew. Chem., Int. Ed.*, 2013, **52**, 8102–8106.
6 S. Zhang, *IEEE Trans. Plasma Sci.*, 2006, **34**, 294–304.
7 B. Dong, J. Wang, J. Sun, S. Xu, X. Bai, Z. Jiang, L. Xia, L. Sun and H. Song, *RSC Adv.*, 2012, **2**, 3897–3905.
8 K. M. Kim and J. H. Ryu, *J. Alloys Compd.*, 2013, **576**, 195–200.
9 I. L. Medintz, H. T. Uyada, E. R. Goldman and H. Mattoussi, *Nat. Mater.*, 2005, **4**, 435–446.
10 H. Dong, L.-D. Sun and C.-H. Yan, *Nanoscale*, 2013, **5**, 5703–5714.
11 V. Bachmann, C. Ronda and A. Meijerink, *Chem. Mater.*, 2009, **21**, 2077–2084.
12 J. Dhanaraj, R. Jagannathan, T. R. N. Kutty and C.-H. Lu, *J. Phys. Chem. B*, 2001, **105**, 11098–11105.
13 J.-G. Li, X. Li, X. Sun and T. Ishigaki, *J. Phys. Chem. C*, 2008, **112**, 11707–11716.
14 C. Guo, L. Luan, C. Chen, D. Huang and Q. Su, *Mater. Lett.*, 2008, **62**, 600–602.
15 J. Kuang, Y. Liu and D. Yuan, *Electrochem. Solid-State Lett.*, 2005, **8**, H72–H74.
16 R. Yu, H. Noh, B. Moon, B. Choi, J. Jeong, K. Jang, S. Yi and J. Jang, *J. Alloys Compd.*, 2013, **576**, 236–241.
17 D. Zou, Y. Q. Ma, S. B. Qian, B. T. Huang, G. H. Zheng and Z. X. Dai, *J. Alloys Compd.*, 2014, **584**, 471–476.
18 L. Jia, Z. Shao, Q. Lü, Y. Tian and J. Han, *Ceram. Int.*, 2014, **40**, 739–743.
19 K. S. Sohn, Y. Y. Choi and H. D. Park, *J. Electrochem. Soc.*, 2000, **147**, 1988–1992.

20 X. Zhang, X. Zhang, Z. Zhao and J. Chauduhuri, *J. Mater. Sci.*, 2015, **50**, 251–257.
21 G. B. Chadeyron, M. E. Ghozzi, D. Boyer, R. Mahiou and J. C. Cousseins, *J. Alloys Compd.*, 2001, **317**, 183–185.
22 J. T. Ingle, R. P. Sonekar, S. K. Omanwar, Y. Wang and L. Zhao, *Combust. Sci. Technol.*, 2014, **186**, 83–89.
23 A. B. Gawande, R. P. Sonekar and S. K. Omanwar, *Combust. Sci. Technol.*, 2014, **186**, 785–791.
24 K. Y. Jung, E. J. Kim and Y. C. Kang, *J. Electrochem. Soc.*, 2004, **151**, H69–H73.
25 N. Joffin, B. Caillier, A. Garcia, P. Guillot, J. Galy, A. Fernandes, R. Mauricot and J. D. Ghys, *Opt. Mater.*, 2006, **28**, 597–601.
26 G. Jia, P. A. Tanner, C. K. Duan and J. D. Ghys, *J. Phys. Chem. C*, 2010, **114**, 2769–2775.
27 K. Y. Jung and H. K. Jung, *J. Lumin.*, 2010, **130**, 1970–1974.
28 D. Boyer, G. B. Chadeyron, R. Mahiou, C. Caperaa and J. C. Cousseins, *J. Mater. Chem.*, 1999, **9**, 211–214.
29 L. Lou, D. Boyer, G. B. Chadeyron, E. Bernstein, R. Mahiou and J. Mugnier, *Opt. Mater.*, 2000, **15**, 1–6.
30 Z. Wei, L. Sun, C. Liao, J. Yin, X. Jiang and C. Yan, *J. Phys. Chem. B*, 2002, **106**, 10610–10617.
31 Z. G. Wei, L. D. Sun, C. S. Liao, X. C. Jiang, C. H. Yan, Y. Tao, X. Y. Hou and X. Ju, *J. Appl. Phys.*, 2003, **93**, 9783–9788.
32 D. Boyer, G. Bertrand and R. Mahiou, *J. Lumin.*, 2003, **104**, 229–237.
33 H. Zhu, L. Zhang, T. Zuo, X. Gu, Z. Wang, L. Zhu and K. Yao, *Appl. Surf. Sci.*, 2008, **254**, 6362–6365.
34 K. N. Kim, H. K. Jung, H. D. Park and D. Kim, *J. Mater. Res.*, 2002, **17**, 907–910.
35 X. C. Jiang, C. H. Yan, L. D. Sun, Z. G. Wei and C. S. Liao, *J. Solid State Chem.*, 2003, **175**, 245–251.
36 R. Sato, S. Takeshita, T. Isobe, T. Sawayama and S. Niikura, *ECS J. Solid State Sci. Technol.*, 2012, **1**, R163–R168.
37 A. Nohara, S. Takeshita and T. Isobe, *RSC Adv.*, 2014, **4**, 11219–11224.
38 A. Nohara, S. Takeshita, Y. Iso and T. Isobe, *J. Mater. Sci.*, 2016, **51**, 3311–3317.
39 A. A. Setlur, *Electrochem. Solid-State Lett.*, 012, **15**, J25–J27.
40 S. Sohal, M. Nazari, X. Zhang, E. Hassanzadeh, V. V. Kuryatkov, J. Chaudhuri, L. J. Hope-Weeks, J. Y. Huang and M. Holtz, *J. Appl. Phys.*, 2014, **115**, 183505.
41 B. Lee, S. Lee, H. G. Jeong and K.-S. Sohn, *ACS Comb. Sci.*, 2011, **13**, 154–158.
42 K. H. Son, S. P. Singh and K.-S. Sohn, *J. Mater. Chem.*, 2012, **17**, 8505–8511.
43 S. P. Singh, W. B. Park, C. Yoon, D. Kim and K.-S. Sohn, *ECS J. Solid State Sci. Technol.*, 2016, **5**, R3032–R3039.
44 W. B. Park, S. P. Singh, M. Kim and K.-S. Sohn, *Inorg. Chem.*, 2015, **4**, 1829–1840.
45 J. W. Park, B. Y. Han, Y. S. Kim and K.-S. Sohn, *J. Nanosci. Nanotechnol.*, 2013, **6**, 3935–3958.
46 T. Chan, C. Kang, R. Liu, L. Chen, X. Liu, J. Ding, J. Bao and C. Gao, *J. Comb. Chem.*, 2007, **9**, 343–346.
47 X. Su, K. Zhang, Q. Liu, H. Zhong, Y. Shi and Y. Pan, *ACS Comb. Sci.*, 2011, **13**, 79–83.
48 B. Bender, C. Condra, R. J. Gould and T. M. Connolly, *Thromb. Res.*, 1995, **77**, 453–463.
49 H. Wang and J. A. Joseph, *Free Radical Biol. Med.*, 1999, **27**, 612–616.
50 M. U. Kassack, B. Hofgan, J. Lehmann, N. Eckstein, J. M. Quillan and W. Sadee, *J. Biomol. Screening*, 2002, **7**, 233–246.
51 X. Zhao, X. Wang, B. Chen, W. Di, Q. Meng and Y. Yang, *Proc. SPIE*, 2006, **6030**, 60300N.
52 X. Zhang, L. Zhou, Q. Pang and M. Gong, *J. Am. Ceram. Soc.*, 2014, **97**, 2124–2129.
53 X. Zhang, L. Zhou, Q. Pang and M. Gong, *Opt. Mater.*, 2014, **36**, 1112–1118.